Title	Viscoelasticity Response during Fibrillation of Amyloid β Peptides on a Quartz-Crystal-Microbalance Biosensor
Author(s)	Lai, Yen Ting; Ogi, Hirotsugu; Noi, Kentaro et al.
Citation	Langmuir. 2018, 34(19), p. 5474-5479
Version Type	AM
URL	https://hdl.handle.net/11094/84143
rights	This document is the Accepted Manuscript version of a Published Work that appeared in final form in Langmuir, © American Chemical Society after peer review and technical editing by the publisher. To access the final edited and published work see https://doi.org/10.1021/acs.langmuir.8b00639.
Note	

Viscoelasticity Response During Fibrillation of Amyloid β Peptides on Quartz Crystal Microbalance Biosensor

Yen-Ting Lai,[†] Hirotsugu Ogi,[*,‡] Kentaro Noi,[‡] and Fumihito Kato[¶]

†*Graduate School of Engineering Science, Osaka University, Toyonaka, Osaka 560-8531, Japan*

‡*Graduate School of Engineering, Osaka University, Suita, Osaka 565-0871, Japan*

¶*Department of Mechanical Engineering, Nippon Institute of Technology, 4-1 Gakuendai, Minamisaitama-gun, Saitama 345-8501, Japan*

E-mail: ogi@prec.eng.osaka-u.ac.jp

Phone: +81-6-6879-7276. Fax: +81-6-6879-7276

Abstract

Unlike previous in-vitro measurements where Aβ aggregation was studied in bulk solutions, we detect the structure change of the Aβ aggregate on the surface of a wireless quartz-crystal-microbalance biosensor, which resembles more closely the aggregation process on the cell membrane. Using a 58-MHz quartz crystal, we monitored changes in the viscoelastic properties of the aggregate formed on the quartz surface from monomers to oligomers and then to fibrils, involving up to the 7^{th} overtone mode (406 MHz). With atomic-force-microscopy observations, we found significant stiffness increase as well as thinning of the protein layer during the structure change from oligomer to fibrils at 20 h, which indicates that the stiffness of the fibril is much higher. Viscoelasticity can provide a significant index of fibrillation and can be useful for evaluating inhibitory medicines in drug development.

INTRODUCTION

Amyloid β (Aβ) peptides consist of 36 to 43 amino-acid sequences, which result from the amyloid precursor protein through the cleaving procedure by β and γ secretases.[1,2] The Aβ peptides relate strongly to pathogenesis of Alzheimer's disease (AD); their aggregates are main components of amyloid plaques in brains of AD patients.[3,4] The Aβ peptides show self-assembling behavior and form the amyloid fibrils through a specific aggregation pathway, involving oligomers. The amyloid fibril is composed of the β-sheet structures and is highly stable,[5] and it is considered as the dead end of the aggregation pathway. The Aβ oligomers appear before the fibril state and therefore are called intermediates of the pathway (Fig. 1). The oligomers,[6,7] and fibrils[8,9] show neurotoxicity, and they are recognized as pathogenicity factors for AD. Therefore, clarifying the transition behavior from oligomers into fibrils is not only helpful in understanding the aggregation mechanism (kinetic study of Aβ fibril formation[10–12]), but also in drug development.[13]

Although the aggregation phenomenon of the Aβ peptides has been studied for decades, the aggregation reactions were usually performed in bulk liquids,[8,10,13–15] where critical problem always arose: the Aβ aggregation reaction in bulk solution proceeds with many interactions among aggregates (monomer, oligomers, and fibrils). These could cause products different from those formed on the surface by the interaction only between monomers and nuclei. Because the in-vivo aggregation reaction proceeds with the deposition of Aβ monomers on the Aβ nuclei immobilized on the membrane surface, it is preferable to study the aggregation reaction on the surface not in the bulk solution.

It is expected that the structural change from oligomers to fibrils will cause significant change in viscoelasticity of the aggregate layer.[16,17] This is because the amyloid fibrils show stiffness much higher than standard protein aggregates.[18] Since a high-frequency quartz crystal microbalance (QCM) is sensitive not only to the mass of the aggregates on the surface but also to their viscoelasticity,[19,20] we expect that such a structural transition can be detected with a high-frequency QCM measurement.

Viscoelastic models in a QCM assay[21–23] have been built for various surroundings such as gas, water,[24,25] and amphiphilic overlayer.[26–28] Most studies have used dissipation of the resonance vibration for this purpose,[29,30] which is, however, affected not only by protein viscoelasticity but also by many ambiguous conditions such as the solution flow rate, the holding condition of the sensor chip, and so on. On the other hand, the frequency change, which can also be used for evaluating the viscoelasticity, is highly stable and much more robust to ambiguous measurement conditions. It is thus desirable to use only the frequency responses, but a QCM with sufficiently higher frequency is needed for this to improve the sensitivity to viscoelasticity.[19]

In this study, the aggregation reaction of Aβ_{1-40} peptide was promoted on a wireless-electrodeless QCM chip packaged in a microchannel, and its progress was monitored in real-time through frequency responses, up to the 7^{th} overtones. (The fundamental resonance frequency of our QCM is about 58 MHz, so that the 7^{th} mode exceeds 400 MHz.) This very-high-frequency QCM improves the mass sensitivity for smaller particles like Aβ (molecular weight: 4,500 Da)[31] and allows determining simultaneously the protein-layer thickness, viscosity, and shear stiffness.

It has been shown that Aβ_{1-42} seeds immobilized on a surface capture Aβ_{1-40} monomers, resulting in oligomeric layers.[32,33] Here, the aggregation reaction of Aβ_{1-40} monomers on the Aβ_{1-42} seeds was then studied. This binding system is practically important for two reasons. First, Aβ_{1-42} peptides show much higher hydrophobicity than Aβ_{1-40}[34] and they easily form the aggregation nuclei on the membrane surface. Second, the number of Aβ_{1-40} are highest in human brain,[35–37] and they will accumulate on the Aβ_{1-42} seeds.

Beside the overtone measurements, we performed the aggregation reaction on a bare quartz crystal without packaging to study the correlation between the viscoelasticity change and the surface morphology with an atomic-force microscope (AFM). We succeed in detecting, for the first time, the stiffening phenomenon in the protein layer after a long lag time on the surface. And we reveal that this stiffening is caused by the transition from oligomers into fibrils.

VISCOELASTIC MODEL

We assume that a continuous and homogenous protein layer grows on the quartz oscillator between the solution layer and quartz surface. The resonance frequency of such a multilayer system principally depends on four parameters: thickness, viscosity, and stiffness of the protein layer, and the overtone index n of the resonance.[19,20,25] We then simultaneously measured the frequency change for n=1, 3, 5, and 7 to extract the remaining three parameters inversely by a the least-squares method.

In the model,[19,20]we assigned different materials to each layer: First, the WE-QCM is regarded as purely elastic (α-quartz). Next, the protein (Aβ) layer is regarded as a viscoelastic Kelvin-Voigt material,[28] where an elastic spring and a dashpot are connected in parallel. Last, the solution layer is considered as a Newtonian fluid. Considering the free boundaries at the upmost and the downmost boundaries, and continuities of stress and displacement at each interface, we obtain the frequency equation and then the frequency change:

$$\Delta f_n \approx \frac{1}{2\pi\rho_q h_q} Im(\kappa_p \xi_p \frac{1 - Ae^{2\xi_p h_p}}{1 + Ae^{2\xi_p h_p}}) \tag{1}$$

where

$$A = \frac{\kappa_p\xi_p + \eta_s\xi_s tanh(\xi_s h_s)}{\kappa_p\xi_p - \eta_s\xi_s tanh(\xi_s h_s)},\ \kappa_p = \frac{\mu_p^*}{j\omega_n}\ ,\ \xi_p = \sqrt{-\frac{\rho_p\omega_n^2}{\mu_p^*}}\ ,\ \xi_s = \sqrt{\frac{j\rho_s\omega_n}{\eta_s}},\ \mu_p^* = \mu_p + j\omega_n\eta_p$$

Here, h, ρ, μ, and η denote thickness, mass density, shear modulus, and viscosity, and ω_n is the angular frequency of the nth overtone. The subscripts s, p, and q represent solution, protein, and quartz layers, respectively. We assumed ρ_p to be 1100 kg/m^3 to reduce the ambiguity of calculation because of its noncritical behavior compared with other parameters.[19] The three parameters (h_p, μ_p, and η_p) are then inversely determined from four overtone frequencies measured simultaneously.

EXPERIMENT

All measurements and sample preparation were done at room temperature.

Preparation of Aβ_{1-42} Seed Solution

Aβ_{1-42} monomer (4349-v, Peptide Institute, Ibaraki, OSAKA, Japan) was dissolved in dimethyl sulfoxide (DMSO) with magnetic stirring for 10 min at 150 rpm. It was then diluted in acetate buffer solution (ABS, pH = 4.6) to a concentration of 50 μM, where the volume ratio of DMSO to ABS was 1 to 5. This seed solution was then stirred for 24 h at 1200 rpm to form the fibrils.[15,32] The solution was then exposed to 200-W ultrasonic irradiation under 26 kHz to fragmentate the fibrils to obtain the seeds. The solution was diluted by ABS to obtain the seed solution with concentration of 16 μM total monomer. The formation of fibril seed was confirmed by thioflavin-T (ThT) fluorescence experiment;[15] the ThT level of the seed solution was higher than that of the monomer solution by a factor of ~100.

Preparation of Aβ_{1-40} Flowing Solution

Aβ_{1-40} monomer (4307-v, Peptide Institute, Ibaraki, OSAKA, Japan) was dissolved in DMSO and was diluted in ultrapure water until a final concentration of 10 μM was reached. The ratio of DMSO to ultrapure water was 1:20. Note that the flowing solution should be prepared right before its injection into the QCM measurement.

Preparation of MEMS QCM Chips

A bare AT-cut quartz chip of 1.7 mm × 2.5 mm with a thickness of 28 μm was placed into the Si microchannel, which was sandwiched by two glass plates as shown in Fig. 2(a). The solution volume is about 0.8 μl, and the quartz crystal was lightly supported with micropillars and walls, without tight clamping (Fig. 2(b)). The package was sealed by an anodic-bonding procedure.[31,38]

The MEMS QCM chip was first washed with piranha solution (7:3 of H_2SO_4 to H_2O_2) for 10 min, rinsed with ultrapure water (until pH 7), and cleaned with UV-ozone for 15 min. It was then immersed with the Aβ_{1-42} seed solution and incubated for $\sim$20 h at 4°C to immobilize the seeds on the quartz crystal by nonspecific adsorption. The chip was washed with ultrapure water and then set into the sensor cell with two flat copper antennas (Fig. 2(b)).

Preparation of Non-packaged WE-QCM

The non-packaged WE-QCM was used to study the surface morphology of the Aβ aggregate using AFM. The bare quartz chip of 1.7 mm x 2.5 mm area and 28 μm thickness was washed with piranha solution for 10 min, rinsed with ultrapure water, and cleaned with UV-ozone for 15 min. Next, the chip was immersed in the Aβ_{1-42} seed solution for 20 h at 4°C. The chip was then sandwiched by silicon rubber sheets and set into the handmade sensor cell with a volume of 0.3 ml, and two antennas were embedded on both sides. Details are given in refs.[39,40]

Experiment Setup for the MEMS QCM for Viscoelasticity

Two flat antennas were connected to a network analyzer (ZNB, ROHDE&SCHWARZ) and the transmission signal (S12) was monitored. A micro-piezoelectric pump was used to induce solution flow.

Initially, ultrapure water flowed into the sensor cell over the quartz surfaces as the carrier solution. When the four frequencies became stable, the Aβ_{1-40} flowing solution was injected with the flow rate 20 μl/min. (The solution would fill the microchannel in 2.4 s.) We monitored the resonance frequencies of the fundamental (58 MHz), 3^{rd} (174 MHz), 5^{th} (290 MHz), and 7^{th} (406 MHz) modes simultaneously.

AFM Observation

The aggregation reaction that occurred on the surface of the non-packaged WE-QCM system was stopped at representative stages (before injection, initial binding, just before the structural transition, and after the structural transition), and AFM images on the quartz-chip were taken. A tapping-mode using a silicon cantilever with a bending stiffness of 40 N/m was used for the measurements. The resonance frequency of the cantilever was near 300 kHz. The scan frequency rate was 1 Hz. The AFM system was produced by Shimadzu Co. Ltd. (SPM A9600).

RESULTS

Overtone Experiment

A typical result for the overtone measurement of Aβ_{1-40} binding to seeds on the MEMS QCM is shown in Figs. 3 (a) and 3 (b). (Other independent experimental results are shown in Supplementary Figure S1.) As shown in Fig. 3 (b), the Aβ_{1-40} flow solution arrives at the sensor chip at time 0, and all overtone frequencies drastically drop by 250-300 ppm within 1 h. Then, the frequencies gradually increase until 18 h with slopes of 2.1, 2.8, 2.5, and 1.7 ppm/h between 10 and 15 h for fundamental, 3^{rd}, 5^{th}, and 7^{th} modes, respectively. However, the resonance frequencies significantly increased between 18 and 20 h (we call this a frequency ramp), and their slopes also increased to 8.0, 6.6, 6.1, and 10 ppm/h, respectively. Afterward, the frequencies became stable again with slopes of 3.0, 3.5, 3.1, and 3.6, respectively.

Viscoelasticity Calculation

Here we evaluate the evolution of thickness (h), viscosity (η), and shear modulus (μ) of the Aβ layer from the four (fundamental, 3^{rd}, 5^{th}, 7^{th}) resonance frequencies using the least-squares method.

Results are shown in Fig. 4 for the experiments in Fig. 3. After a few minutes from the arrival of the solution at the quartz surfaces, the thickness increases up to about 12 nm (Fig. 4(b)), and then decreases gradually. Its decremental rate, however, raises between 18 and 21 h (Fig. 4(c)). A similar trend is observed in the viscosity change (Figs. 4(b) and 4(d)). The shear modulus increases at first (Fig. 4(b)), then gradually decreases, and increases again between 18 and 21 h (Fig. 4(e)). The viscosity and the shear modulus change in a different direction in the period between 18 and 21 h.

Correlation Between Frequency Change and Surface Structure

Figures 5 (a)-(d) show a series of independent QCM experimental results, and Figures 5 (e)-(i) show their corresponding AFM images. (AFM images for other experiments are shown in Supplementary Figures S2 and S3) Before the injection (0 h), we see many dots with ∼100-nm diameters (Fig. 5 (e)), indicating immobilized Aβ_{1-42} seeds on the WE-QCM surface. After a few minutes of the injection (0.5 h), the frequency dropped (Fig. 5 (a)), and the corresponding AFM image, Fig. 5 (f), shows larger particles than those seen at 0 h. The measurement in Fig. 5 (b) shows the gradual increase of the frequency after the initial binding. The AFM image at 15 h (before the ramp) shows many amorphous-like structures, where the particles grew bigger than before (Fig. 5 (g)). In Fig. 5 (c), the ramp appears at 24.5 h where the slope increased from 0.5 to 15 ppm/h (see the enlarged figure). Fig. 5 (d) confirms the observation of the ramp in another independent experiment at ∼20 h. The AFM images after the ramp clearly show many fine fibrils in the entire region of the quartz surfaces (Fig. 5 (h) and Fig. 5 (i)). Therefore, the frequency ramp near 20 h indicates the transition from oligomers to amyloid fibrils.

DISCUSSION

In considering the time-dependent evolution of the viscoelastic parameters and surface structure, we separate the results into three phases. First is the binding phase. It is the period starting from the injection of monomer solution until the maximum frequency decrement is reached. Second is the lag phase, which is the long and relatively stable interval from 0.5 h (after the binding phase) to ∼18 h (before the frequency ramp). Last is the transition phase from 18 to 20 h in case of Fig. 3 (a).

Before the arrival of the $A\beta_{1-40}$ flowing solution, we see dots with diameters of about ∼100-nm on the quartz surface in the AFM image (Fig. 5(e)), which we recognize as $A\beta_{1-42}$ seeds immobilized on the quartz chip. In the binding phase, the significant drops in the frequencies cause a large increase in the thickness, viscosity, and shear modulus in the $A\beta$ layer (Fig. 3(b) and Fig. 4(b)), indicating that the flowing $A\beta_{1-40}$ monomers are captured by the $A\beta_{1-42}$ seeds, making the layer thicker and stiffer.

In the early stage of the lag phase (from 1 to 6 h in Fig. 4(a)), the frequencies increase and the thickness decreases, and one may attribute these changes to the detachment of weakly captured monomers from the surface. However, this would not be a principal cause because the viscosity and shear modulus remain unchanged in this period (Fig. 4(a) and 4(b)); our QCM sensing region is about 20 nm from surface,[19] and the averaged shear modulus and viscosity in this region are deduced from the inverse calculation. Because the parameters (stiffness, viscosity, and thickness) depend on the body layer of the system, they should be taken in to account together. From the binding-phase response ($<\sim$0.5 h), it is expected that the three parameters increase simultaneously when monomers attach to the seeds immobilized on sensor surface. Therefore, detachment of monomers should make all three parameters drop. However, the stable viscoelastic properties (shear modulus and viscosity) contradict this prediction. Therefore, the unchanged average shear modulus and viscosity with decrease in the thickness of the adlayer indicates increases in the stiffness and viscosity of the protein aggregates. It is also shown in Ref. 33 that the $A\beta$ particle size increases gradually on the surface, which contradicts detachment of weakly captured monomers from the surface. Thus, we consider that the condensation of Aβ aggregates occurs in this period.

After this period in the lag phase, both thickness and shear modulus decrease gradually, while the viscosity remains unchanged until just before the ramp (Fig. 3(a) and Fig. 4(b)). We consider that Aβ capturing and aggregate condensation[33] continue during this period. Unchanged viscosity again argues against the contribution of detachment of monomers. The shear-modulus decrease suggests that the protein stiffness is nearly unchanged during this period, so that the averaged modulus gradually decreased. This view is confirmed by AFM images (Fig. 5 (g)) which show that the aggregates grow on the quartz surface; the deposited Aβ peptides continue to form dense aggregates, but their structure is not yet fibril.

At the transition phase (18 to 21 h in Fig. 3(a) and Fig. 4 (c)-(e)), a larger increase, compared to the lag phase, occurred in frequency slopes, which results in the stiffness increase and the thickness decrease. This indicates the transition from oligomer to fibril because amyloid fibrils show stiffness much higher than standard protein aggregates.[18] It is verified by AFM images shown in Figs. 5(h) and (i), where dense aggregate structures are replaced by fibril-like structures. Because we failed to find any fibrils just before the ramp, we think that fibrillation occurs simultaneously over nearly the whole area of the quartz crystal. (As shown in Supplementary Figure S4, the dense fibril structure was observed in different areas of the quartz chip after the ramp.) The significant decrease of the Aβ layer thickness in the phase can be caused by the ordering of the aggregates to form the dense fibril. The average shear modulus simultaneously increases, reflecting the much higher stiffness of the formed fibrils. Furthermore, the stiffness increase is also enhanced by the formation of the cross-networking fibril structure as shown in the AFM images (Fig. 5h, 5i and Fig. S3b and S3c).

The viscoelastic model used in this work is greatly simplified; the model regards the Aβ layer as a continuous and homogenous layer despite the fact that the protein layer includes not only the aggregates but also the surrounding solution. However, because the viscoelasticity of the aggregate significantly changes, the overall property of the protein layer will be sufficiently affected. The mechanical properties related to the fibril formation can then be evaluated even macroscopically, providing a significant insight. A more appropriate mode, which considers the island growth of Aβ aggregates around specifically adsorbed nuclei, will be developed in our future studies.

CONCLUSIONS

Analysis of Aβ aggregation was carried out on a quartz surface and the conformational change correlation to frequency response was verified by AFM. It is a label-free methodology of monitoring the mechanical variation of adsorbed proteins on the surface in real time. The viscoelasticity model of Aβ aggregation was successfully established, where we were able to characterize Aβ aggregation in detail, showing it to be a decisive method for analyzing the aggregation phenomenon. The model may be applied in further analysis of other fibrillation characteristics, such as duration, rate and interval of the fibrillation upon introduction of impurities such as inhibitors and different solvents.

AUTHOR INFORMATION

Corresponding Authors

*E-mail ogi@prec.eng.osaka-u.ac.jp (H. O.).

Author Contributions

Y.-T. L. performed overtone and correlation experiments, viscoelasticity calculation and wrote this paper. H. O. invented the WE-QCM system, produced this study and wrote paper. N. K. prepared the solutions and fabricated the MEMS-QCM. K. F. fabricated the MEMS QCM.

ABBREVIATIONS

ABS, acetate buffer solution; Aβ, amyloid β; AD, Alzheimer's disease; AFM, atomic force microscopy; DMSO, dimethyl fluoride; ThT, thioflavin-T; MEMS, micro-electromechanical system; WE-QCM, wireless-electrodeless quartz crystal microbalance

Acknowledgement

This study is partially supported by Development of Advanced Measurement and Analysis Systems from Japan Science and Technology Agency, JST.

References

(1) Vassar, R.; Bennett, B.; Babu-Khan, S. ; Kahn, S.; Mendiaz, E.; Denis, P.; Teplow, D.; Ross, S.; Amarante, P.; Loeloff, R.; Luo, Y.; Fisher, S.; Fuller, J.; Edenson, S.; Lile, J.; Jarosinski, M.; Biere, A.; Curran, E.; Burgess, T.; Louis, J.-C.; Collins, F.; Treanor, J.; Rogers, G.; Citron, M. β-Secretase Cleavage of Alzheimer's Amyloid Precursor Protein by the Transmembrane Aspartic Protease BACE. *Science* **1999**, *286*, 735-741.

(2) LaFerla, F. M.; Green, K. N.; Oddo, S. Intracellular Amyloid-β in Alzheimer?s disease. *Nat. Rev. Neurosci.* **2007**, *8*, 499-509.

(3) Glenner, G. G.; Wong, C. W. Alzheimer?s Disease: Initial Report of the Purification and Characterization of a Novel Cerebrovascular Amyloid Protein. *Biochem. Biophys. Res. Commun.* **1984**, *120*, 885-890.

(4) Bucciantini, M.; Giannoni, E.; Chiti, F.; Baroni, F.; Formigli, L.; Zurdo, J.; Taddei, N.; Ramponi, G.; Dobson, C. M.; Stefani, M. Inherent Toxicity of Aggregates Implies a Common Mechanism for Protein Misfolding Diseases. *Nature* **2002**, *416*, 507-511.

(5) Lührs, T.; Ritter, C.; Adrian, M.; Riek-Loher, D.; Bohrmann, B.; Döbeli, H.; Schubert, D.; Riek, R. 3D Structure of Alzheimer's amyloid-β(1-42) fibrils. *Proc. Natl. Acad. Sci. U.S.A.* **2005**, *102*, 17342-17347.

(6) Lambert, M. P.; Barlow, A. K.; Chromy, B. A.; Edwards, C.; Freed, R.; Liosatos, M.; Morgan, T. E.; Rozovsky, I.; Trommer, B.; Viola, K. L.; Wals, P.; Zhang, C.; Finch, C. E.; Krafft, G. A.; Klein, W. L. Diffusible, Nonfibrillar Ligands Derived From Aβ_{1-42} are Potent Central Nervous System Neurotoxins. *Proc. Natl. Acad. Sci. U.S.A.* **1998**, *95*, 6448-6453.

(7) Petkova, A. T.; Leapman, R. D.; Guo, Z.; Yau, W.-M.; Mattson, M. P.; Tycko, R. Self-Propagating, Molecular-Level Polymorphism in Alzheimer's β-Amyloid Fibrils. *Science* **2005**, *307*, 262-265.

(8) Langer, F.; Eisele, Y. S.; Fritschi, S. K.; Staufenbiel, M.; Walker, L. C.; Jucker, M. Soluble Aβ Seeds Are Potent Inducers of Cerebral β-Amyloid Deposition. *J. Neurosci.* **2011**, *31*, 14488-14495.

(9) Qiang, W.; Yau, W.-M.; Lu, J.-X.; Collinge, J.; Tycko, R. Structural Variation in Amyloid-β Fibrils from Alzheimer's Disease Clinical Subtypes. *Nature* **2017**, *541*, 217-221.

(10) Nilssonm, M. R. Techniques to Study Amyloid Fibril Formation in Vitro. *Methods* **2004**, *34*, 151-160.

(11) Kotarek, J. A.; Johnson, K. C.; Moss, M. A. Quartz Crystal Microbalance Analysis of Growth Kinetics for Aggregation Intermediates of the Amyloid-β Protein. *Anal. Biochem.* **2008**, *378*, 15-24.

(12) Knowles, T. P. J.; Shu, W.; Devlin, G. L.; Meehan, S.; Auer, S.; Dobson, C. M.; Welland, M. E. Kinetics and Thermodynamics of Amyloid Formation from Direct Measurements of Fluctuations in Fibril Mass. *Proc. Natl. Acad. Sci. U.S.A.* **2007**, *104*, 10016-10021.

(13) Soto, C.; Sigurdsson, E. M.; Morelli, L.; Kumar, R. A.; Castaño, E. M.; Frangione, B. β-sheet Breaker Peptides Inhibit Fibrillogenesis in a Rat Brain Model of Amyloidosis: Implication for Alzheimer's Therapy. *Nat. Med.* **1998**, *4*, 822-826.

(14) Yoshimura, Y.; Lin, Y.; Yagi, H.; Lee, Y.-H.; Kitayama, H.; Sakurai, K.; So, M.; Ogi, H.; Naiki, H.; Goto, Y. Distinguishing Crystal-Like Amyloid Fibrils and Glass-Like Amorphous Aggregates from Their Kinetics of Formation. *Proc. Natl. Acad. Sci. U.S.A.* **2012**, *109*, 14446-14451.

(15) Nakajima, K.; Ogi, H.; Adachi, K.; Noi, K.; Hirao, M.; Yagi, H.; Goto, Y. Nucleus Factory on Cavitation Bubble for Amyloid β Fibril. *Sci. Rep.* **2016**, *6*, 22015.

(16) Bernstein, S. L.; Dupuis, N. F.; Lazo, N. D.; Wyttenbach, T.; Condron, M. M.; Bitan, G.; Teplow, D. B.; Shea, J.-E.; Ruotolo, B. T.; Robinson, C. V.; Bowers, M. T. Amyloid-β Protein Oligomerization and the Importance of Tetramers and Dodecamers in the Aetiology of Alzheimer's disease. *Nat. Chem.* **2009**, *1*, 326-331.

(17) Lee, J.; Culyba, E. K.; Powers, E. T.; Kelly, J. W. Amyloid–β Forms Fibrils by Nucleated Conformational Conversion of Oligomers. *Nat. Chem. Biol.* **2011**, *7*, 602-609.

(18) Smith, J. F.; Knowles, T. P. J.; Dobson, C. M.; MacPhee, C. E.; Welland, M. E. Characterization of the Nanoscale Properties of Individual Amyloid Fibrils. *Proc. Natl. Acad. Sci. U.S.A.* **2006**, *103*, 15806-15811.

(19) Shagawa, T.; Torii, H.; Kato, F.; Ogi, H.; Hirao, M. Viscoelasticity Evolution in Protein Layers During Binding Reactions Evaluated Using High-Frequency Wireless and Elec-

trodeless Quartz Crystal Microbalance Biosensor Without Dissipation. *Jpn. J. Appl. Phys.* **2015**, *54*, 096601.

(20) Shagawa, T.; Torii, H.; Kato, F.; Ogi, H.; Hirao, M. Relationship Between Viscosity Change and Specificity in Protein Binding Reaction Studied by High-Frequency Wireless and Electrodeless MEMS Biosensor. *Jpn. J. Appl. Phys.* **2015**, *54*, 068001.

(21) Voinova, M. V.; Jonson, M.; Kasemo, B. 'Missing Mass' Effect in Biosensor's QCM Applications. *Biosens. Bioelectron.* **2002**, *17*, 835 -841.

(22) Rodahl, M.; Kasemo, B. On the Measurement of Thin Liquid Overlayers with the Quartz-Crystal Microbalance. *Sens. Actuators, A* **1996**, *54*, 448-456.

(23) Kanazawa, K.; Gordon II, J. G. The Oscillation Frequency of a Quartz Resonator in Contact with a Liquid. *Anal. Chmi. Acta* **1985**, *175*, 99-105.

(24) Rodahl, M.; Höök, F.; Krozer, A.; Brzezinski, P.; Kasemo, B. Quartz Crystal Microbalance Setup for Frequency and Q-Factor Measurements in Gaseous and Liquid Environments. *Rev. Sci. Instrum.* **1995**, *66*, 3924-3930.

(25) Höök, F.; Kasemo, B.; Nylander, T.; Fant, C.; Sott, K.; Elwing, H. Variations in Coupled Water, Viscoelastic Properties, and Film Thickness of a Mefp-1 Protein Film During Adsorption and Cross-Linking: A Quartz Crystal Microbalance with Dissipation Monitoring, Ellipsometry, and Surface Plasmon Resonance Study. *Anal. Chem.* **2001**, *73*, 5796-5804.

(26) Voinova, M. V.; Jonson, M.; Kasemo, B. Dynamics of Viscous Amphiphilic Films Supported by Elastic Solid Substrates. *J. Phys. Condens. Matter* **1997**, *9*, 7799-7808.

(27) Reed, C.; Kanazawa, K.; Kaufman, J. H. Physical Description of a Viscoelastically Loaded AT-Cut Quartz Resonator. *J. Appl. Phys.* **1990**, *68*, 1993-2001.

(28) Voinova, M. V.; Rodahl, M.; Jonson, M.; Kasemo, B. Viscoelastic Acoustic Response of Layered Polymer Films at Fluid-Solid Interfaces: Continuum Mechanics Approach. *Phys. Scr.* **1999**, *59*, 391-396.

(29) Patel, A.; Kanazawa, K.; Frank, C. W. Antibody Binding to a Tethered Vesicle Assembly Using QCM-D. *Anal. Chem.* **2009**, *81*, 6021-6029.

(30) Yan, M.; Liu, C.; Wang, D.; Ni, J.; Chang, J. Characterization of Adsorption of Humic Acid onto Alumina Using Quartz Crystal Microbalance with Dissipation. *Langmuir* **2011**, *27*, 9860-9865.

(31) Ogi, H. Wireless-Electrodeless Quartz-Crystal-Microbalance Biosensors for Studying Interactions Among Biomolecules: A Review. *Proc. Jpn. Acad., Ser. B* **2013**, *89*, 401-417.

(32) Ogi, H.; Fukunishi, Y.; Yanagida, T.; Yagi, H.; Goto, Y.; Fukushima, M.; Uesugi, K.; Hirao, M. Seed-Dependent Deposition Behavior of Aβ Peptides Studied with Wireless Quartz-Crystal-Microbalance Biosensor. *Anal. Chem.* **2011**, *83*, 4982-4988.

(33) Ogi, H.; Fukukshima, M.; Hamada, H.; Noi, K.; Hirao, M.; Yagi, H.; Goto, Y. Ultrafast Propagation of β-Amyloid Fibrils in Oligomeric Cloud. *Sci. Rep.* **2014**, *4*, 6960.

(34) Iwatsubo, T.; Odaka, A.; Suzuki, N.; Mizusawa, H.; Nukina, N.; Ihara, Y. Visualization of Aβ42(43) and Aβ40 in Senile Plaques with End-Specific Aβ Monoclonals: Evidence That an Initially Deposited Species is Aβ42(43). *Neuron* **1994**, *13*, 45-53.

(35) Gravina, S. A.; Ho, L. B.; Eckman, C. B.; Long, K. E.; Otvos Jr., L.; Younkin, L. H.; Suzuki, N.; Younkin, S. G. Amyloid β Protein (Aβ) in Alzheimer's Disease Brain. *J. Biol. Chem.* **1995**, *270*, 7013-7016.

(36) Jarrett, J. T.; Berger, E. P.; Lansbury Jr., P. T. The Carboxy Terminus of the β

Amyloid Protein Is Critical for the Seeding of Amyloid Formation: Implications for the Pathogenesis of Alzheimer's Disease. *Biochemistry* **1993**, *32*, 4693-4697.

(37) Suzuki, N.; Cheung, T. T.; Cai, X. D.; Odaka, A.; Otvos Jr, L.; Eckman, C.; Golde, T. E.; Younkin, S. G. An Increased Percentage of Long Amyloid Beta Protein Secreted by Familial Amyloid Beta Protein Precursor (BetaAPP717) Mutants. *Science* **1994**, *264*, 1336-1340.

(38) Kato, F.; Ogi, H.; Yanagida, T.; Nishikawa, S.; Nishiyama, M.; Hirao, M. High-Frequency Electrodeless Quartz Crystal Microbalance Chip with a Bare Quartz Resonator Encapsulated in a Silicon Microchannel. *Jpn. J. Appl. Phys.* **2011**, *50*, 07HD03.

(39) Ogi, H.; Nagai, H.; Fukunishi, Y.; Hirao, M.; Nishiyama, M. 170-MHz Electrodeless Quartz Crystal Microbalance Biosensor: Capability and Limitation of Higher Frequency Measurement. *Anal. Chem.* **2009**, *81*, 8068-8073.

(40) Ogi, H.; Motohisa, K.; Hatanaka, K.; Ohmori, T.; Hirao, M.; Nishiyama, M. Concentration Dependence of IgG?Protein A Affinity Studied by Wireless-Electrodeless QCM. *Biosens. Bioelectron.* **2007**, *22*, 3238-3242.

Supporting Information Available

- Supplementary Figures: Showing 3 more overtone experiments, 2 more non-packaged-QCM experiments, and a few extra AFM images.

This material is available free of charge via the Internet at `http://pubs.acs.org/`.

Figure Captions

Fig. 1. Typical aggregation pathway of Aβ peptide from monomer to fibril dead end.

Fig. 2. (a) Appearance of the wireless MEMS QCM before the packaging. (b) Mechanism of wireless excitation and detection of the packaged MEMS QCM via the flat antennas through the electromagnetic wave (EM).

Fig. 3. Overtone experiment for fundamental, 3^{rd}, 5^{th}, and 7^{th} modes under Aβ_{1-40} monomer-solution flow over the seeds immobilized on the packaged MEMS QCM. (a) Entire experimental results, with the dashed line indicating the frequency ramp. (b) A close-up figure of (a). (c) The possible structural change on surface.

Fig. 4. (a) Evolutions of layer thickness, viscosity, and shear modulus of Aβ layer derived from the results in Fig. 3. (b) Their changes in the early stage. (c), (d), and (e) show changes of thickness, viscosity, and shear modulus at the transition phase.

Fig. 5. WE-QCM experimental results with only the fundamental mode stopped at (a) 0.5 h, (b) 15 h, (c) 28 h. (d) shows another experiment focusing at the frequency ramp. Note that these are completely independent measurements. (e) shows an AFM image before the injection, and (f)-(i) are AFM images taken after the experiments (a)-(d), respectively.

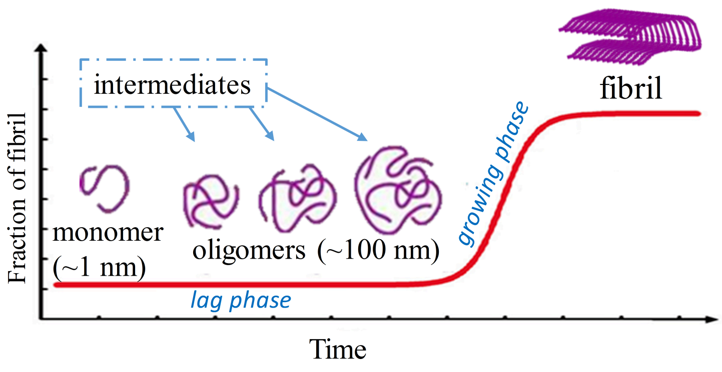
intermediates
fibril
growing phase
monomer
(~1 nm)
oligomers (~100 nm)
lag phase
Fraction of fibril
Time

Figure 1

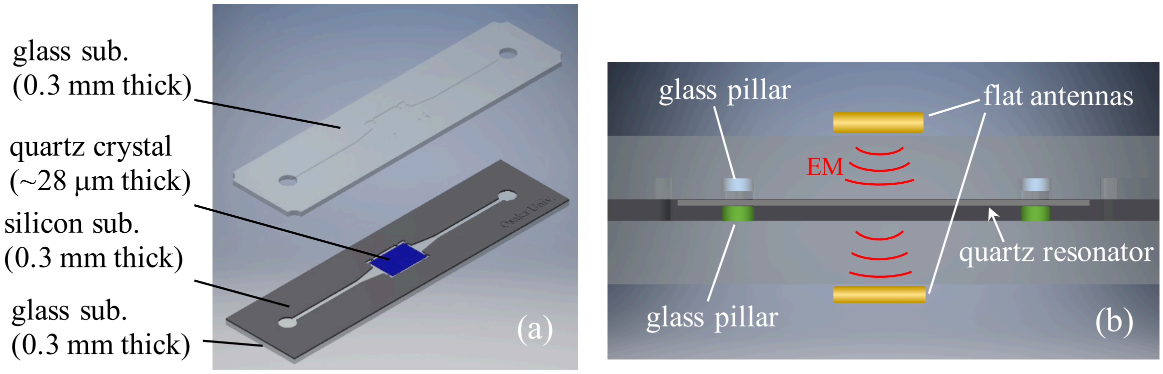
glass sub.
(0.3 mm thick)
quartz crystal
(~28 μm thick)
silicon sub.
(0.3 mm thick)
glass sub.
(0.3 mm thick)
(a)
glass pillar
flat antennas
EM
quartz resonator
glass pillar
(b)

Figure 2

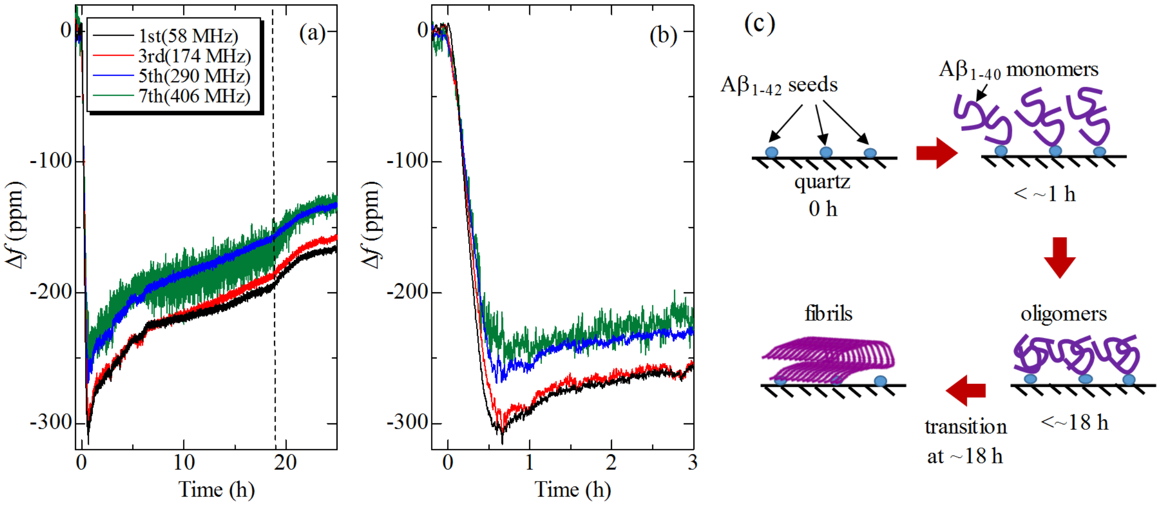
(a)
1st(58 MHz)
3rd(174 MHz)
5th(290 MHz)
7th(406 MHz)
Δf (ppm)
0
-100
-200
-300
0
10
20
Time (h)
(b)
Δf (ppm)
0
-100
-200
-300
0
1
2
3
Time (h)
(c)
Aβ1-42 seeds
quartz
0 h
Aβ1-40 monomers
< ~1 h
oligomers
<~18 h
transition
at ~18 h
fibrils

Figure 3

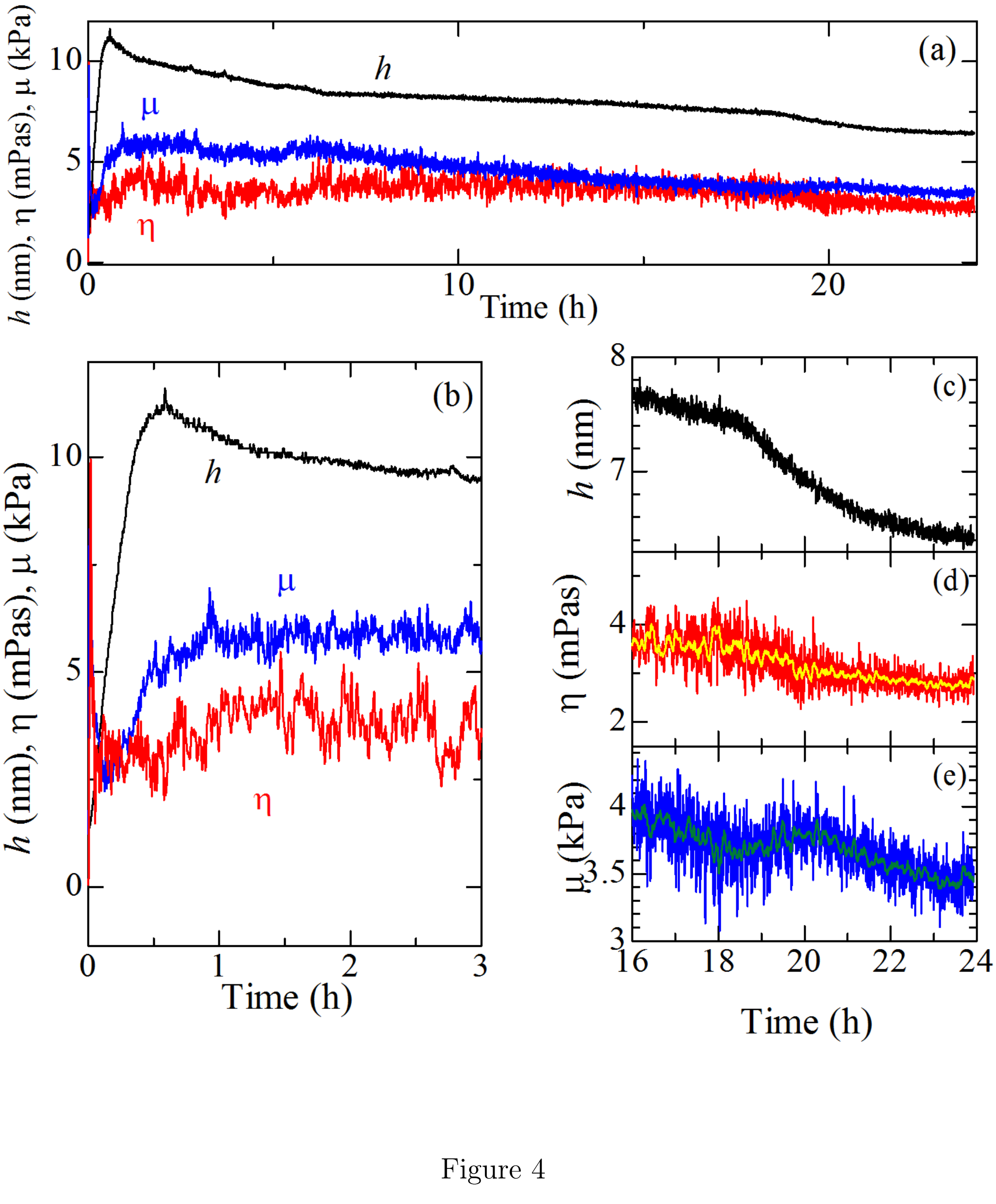
(a)
h
μ
η
h (nm), η (mPas), μ (kPa)
0
5
10
0
10
20
Time (h)
(b)
h
μ
η
h (nm), η (mPas), μ (kPa)
0
5
10
0
1
2
3
Time (h)
(c)
h (nm)
7
8
(d)
η (mPas)
2
4
(e)
μ (kPa)
3
3.5
4
16
18
20
22
24
Time (h)

Figure 4

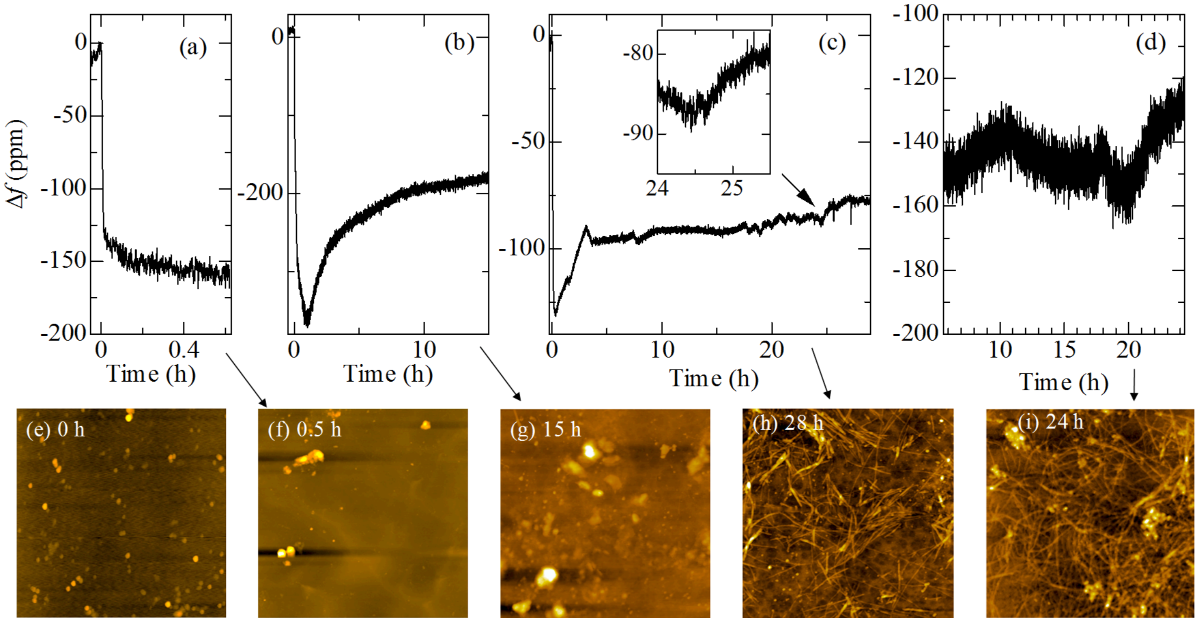
(a)
(b)
(c)
(d)
Δf (ppm)
0
-50
-100
-150
-200
0
0.4
Time (h)
0
-200
0
10
Time (h)
0
-50
-100
0
10
20
Time (h)
-80
-90
24
25
-100
-120
-140
-160
-180
-200
10
15
20
Time (h)
(e) 0 h
(f) 0.5 h
(g) 15 h
(h) 28 h
(i) 24 h

Figure 5

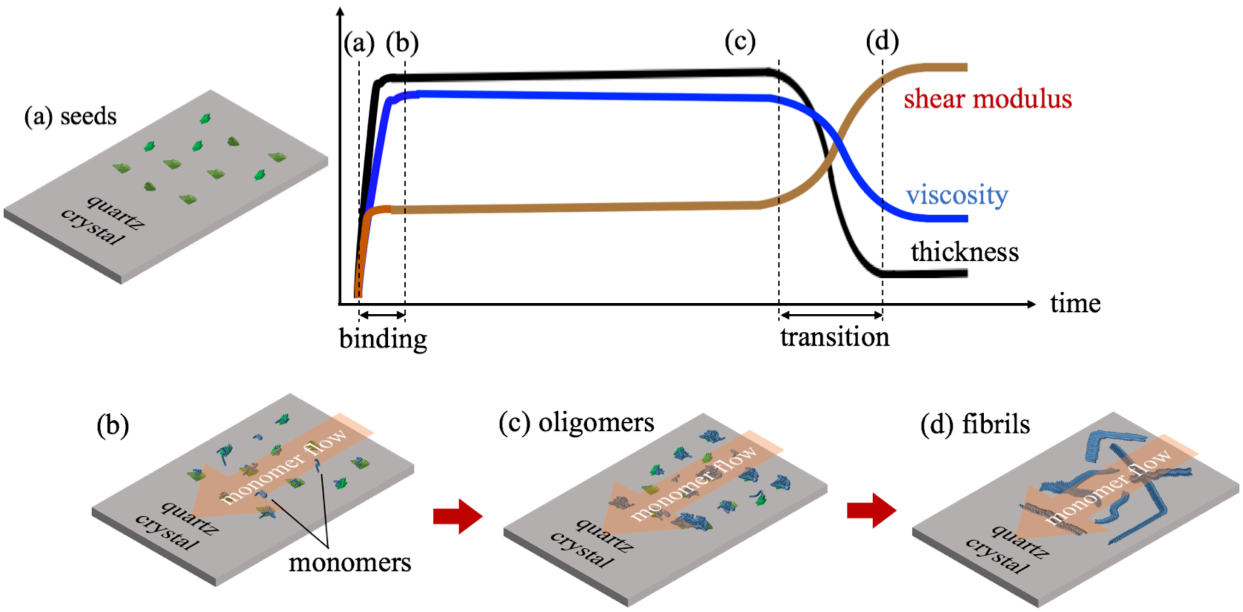
(a) seeds
quartz crystal
(a)
(b)
(c)
(d)
shear modulus
viscosity
thickness
time
binding
transition
(b)
monomer flow
quartz crystal
monomers
(c) oligomers
monomer flow
quartz crystal
(d) fibrils
monomer flow
quartz crystal

TOCgraphic